PHOTONICS Research

Detection of per- and polyfluoroalkyl water contaminants with a multiplexed 4D microcavities sensor

Anton V. Saetchnikov,[1,*] Elina A. Tcherniavskaia,[2] Vladimir A. Saetchnikov,[3] and Andreas Ostendorf[1]

[1]Chair of Applied Laser Technologies, Ruhr University Bochum, 44801 Bochum, Germany
[2]Physics Department, Belarusian State University, 220030 Minsk, Belarus
[3]Radio Physics Department, Belarusian State University, 220064 Minsk, Belarus
*Corresponding author: anton.saetchnikov@rub.de

Received 1 June 2023; revised 3 August 2023; accepted 1 September 2023; posted 5 September 2023 (Doc. ID 496737); published 1 November 2023

The per- and polyfluoroalkyl substances (PFAS) are a group of organofluorine chemicals treated as the emerging pollutants that are currently of particularly acute concern. These compounds have been employed intensively as surfactants over multiple decades and are already to be found in surface and ground waters at amounts sufficient to have an effect on human health and ecosystems. Because of the carbon–fluorine bonds, the PFAS have an extreme environmental persistence and their negative impact accumulates with further production and penetration into the environment. In Germany alone, more than thousands of sites have been identified as contaminated with PFAS; thus, timely detection of PFAS residue is becoming a high priority. In this paper, we report on the high performance optical detection method based on whispering gallery mode (WGM) microcavities applied for the first time to detect PFAS contaminants in aqueous solutions. A self-sensing boosted 4D microcavity fabricated with two-photon polymerization is employed as an individual sensing unit. In an example of the multiplexed imaging sensor with multiple hundreds of simultaneously interrogated microcavities we demonstrate the possibility to detect the PFAS chemicals representatives at a level down to 1 ppb (parts per billion).

https://doi.org/10.1364/PRJ.496737

1. INTRODUCTION

A broad family of organofluorine contaminants known as per- and polyfluoroalkyl substances (PFAS) is a group of more than 10,000 engineered chemicals. They consist of a fully or partially fluorinated carbon chain of various lengths with different functional groups (predominantly carboxylate or sulfonate). These substances are water-, grease-, and dirt-repelling agents that have been vastly used during the last four decades as surfactants in numerous consumer products. Existence of the fluoroalkyl tail, strong carbon–fluorine bond, and exceptionally high thermal and chemical stability prevent PFAS from degrading via water, light, or bacteria. For this reason, PFAS have been classified as persistent organic pollutants and the more they are produced and enter the environment, the more they accumulate. PFAS have already penetrated into the soil, atmosphere, and groundwater and therefore have become hazardous for the ecosystems, biodiversity, and human health [1,2]. Numerous studies show potential immunotoxicity of the PFAS chemicals, their carcinogenicity, effect on fertility, and interaction with hormonal systems [3]. The above-mentioned has prioritized PFAS chemicals for complete elimination.

Traditional analytical approaches such as chromatography (HPLC) or gas (GS) coupled with mass spectrometry (MS) are the most common methods to detect PFAS at concentrations down to ng/L [4,5]. These techniques have excellent performance in terms of accuracy, precision, intrinsic multiplexity, and specificity. However, they suffer from apparatus cost and complexity, the need for laboratory conditions and skilled personnel, and time-consuming processes for sample preparation and data collection. To address these drawbacks, a quick, straightforward, and sensitive technique for PFAS chemical detection is required. An appropriate alternative to the conventional laboratory devices can be provided by biochemical sensors, which are based on various physical principles and offer improved selectivity, flexibility, and compactness for real-time online monitoring. Among them, optical sensors with their high efficiency of light–matter interaction and electromagnetic interference immunity are worthy of special attention. Optical

sensor-based solutions for PFAS detection reported so far are based on fiber/waveguide-based configurations using surface plasmon resonance (SPR) [6–8], lossy mode resonance [9], and interferometric schemes [10]. Particular solutions employ functional layers out of polyvinylidene fluoride [10], antibodies [7], serum albumin [9], or molecularly imprinted polymers [6,8] for enhanced PFAS sensitivity.

Although fiber/waveguide sensor-based configurations provide a low detection limit [reported from ∼0.1 ppb (parts per billion), to several parts per million (ppm)], their sensitivity remains restricted by the limited interaction length between the evanescent field of the guided mode and chemical compounds, where the major part of the evanescent tail remains unaffected and hence does not contribute to the signal. The sensing capability is enhanced when the fiber/waveguide-based detection is realized within an interferometric scheme to enable quantification of the optical field phase changes at the cost of the detection principle complexity. In the SPR-based approach, the metal surfaces are strongly influenced by temperature variations and due to high absorption the surface plasmon wave attenuates rapidly in the propagation direction, limiting the interaction length even more than in fiber/waveguide-based configurations. Here, a competitive alternative for PFAS chemical detection is the optical microresonator-based sensing, where the optical field interaction length with the measured solution is orders of magnitude higher.

For optical microresonators, the electromagnetic (EM) field is trapped by the contrast in refractive indices inside the dielectric material with a closed circular loop [11,12]. For waves that travel along the cavity's edge and interfere with each other after a single roundtrip, the field accumulates in the cavity. Whispering gallery mode (WGM) resonances are the eigenmodes that satisfy the constructive interference condition. These resonances are characterized by the low roundtrip energy dissipation and correspondingly by high quality factors (Q factors) [13]. Due to the presence of the evanescent field outside the cavity geometry, the WGM's spectral properties become susceptible to changes of morphology, material, and/or the geometry of the resonator as well as variations in the environment [14–16].

Microresonator-based sensing technology has undergone significant advancements over the last decades that enabled the sensing of different physical and chemical parameters [17–22], with possibility for deep-learning-powered multiplexed sensing of hundreds or even thousands of resonators [23,24]. Since the first demonstration of biochemical sensing with WGM microresonators [25] multiple different method extensions have been proposed to further boost the sensitivity. Among them are the plasmonic-photonic scheme [26,27], activation (doping cavity with gain medium) [28,29], exceptional points [30], and material response-enhanced sensing by realization of 4D structure-based sensing [31]. The appropriate 4D structures can be fabricated by means of 4D printing technology, where common 3D printing is used to create structures that can react on external disturbances over time. This induced post-manufacturing temporal behavior provides the extra dimension and is enabled by utilization of smart, i.e., stimuli-responsive, materials (commonly hydrogels and polymers) for the manufacturing process [32]. In this way, the function or shape of the fabricated structure varies with respect to the external environment changes, e.g., temperature, humidity, liquid, light, electric field, ionic strength, pH, and chemical composition. The responses of 4D structures are typically divided into self-assembling, self-actuating, and self-sensing [33]. The 4D microresonator-based sensing employs the self-sensing phenomenon that can be initiated under external stimuli on 3D microresonators manufactured with two-photon polymerization (2PP) [34].

As a result, the spectral response of the sensor becomes amplified by the induced reversible variations of the resonator and can be tracked within the WGM detection scheme at high precision. Nevertheless, to the best of our knowledge, and despite numerous benefits over other optical sensing techniques [35], microresonator-based detection has not been employed for PFAS detection so far.

In this paper, we report on the detection of PFAS chemicals in water using the optical microresonators sensing approach demonstrated for the first time to the best of our knowledge. The WGM-based detection is realized in the multiplexed imaging configuration with 4D microresonators as individual sensing units. To gain the high sensing performance, an approach that allocates the water-matched subwavelength film onto the substrate prior to two-photon polymerization is proposed and the impact of the deposited layer onto the sensor fabrication process is numerically studied. We demonstrate that the pre-processed substrate enables enhancement of the loaded Q-factor of 2PP microresonator in the water up to 10^5. Thanks to the self-sensing phenomenon of the resonator photoresin the spectral response of the multiplexed microcavity detector improves by orders of magnitude relative to pure evanescent field sensing. PFAS detection using the 4D microresonators-based approach is validated with examples of two anionic contaminants with carboxylate or sulfonate polar groups and different chain lengths. We demonstrate that the responses of the multiplexed 4D microresonator sensor on at least 10 ppb of perfluorooctanoic acid (PFOA) and 1 ppb of perfluorobutanesulfonic acid (PFBS) clearly stand out relative to the water without the use of any functional layers.

2. MATERIALS AND METHODS

A. Chemicals

Sol-gel SZ2080 photoresin combined with a 4,4′-bis-(diethylamino)-benzophenon photoinitiator and another monomer, 2-(dimethylamino) ethyl methacrylate (DMAEMA), provided by the Foundation for Research and Technology–Hellas (FORTH) was selected for fabrication of the microcavity sensors [36]. The second monomer in this composition serves as a radical quencher throughout the polymerization process to realize the diffusion-assisted 2PP. Ultralow shrinkage, excellent mechanical and chemical stability, a low proximity effect, biocompatibility, good optical quality, high transparency, and ease in preparation, modification, and processing are distinctive features of SZ2080. Phosphate buffer saline (PBS) was prepared in the deionized water, yielding a 0.01 mol/L phosphate buffer, 0.0027 mol/L potassium chloride and 0.137 mol/L sodium chloride, pH 7.4, at 25°C. Perfluorooctanoic acid (PFOA)

and perfluorobutanesulfonic acid (PFBS) of analytical grade were purchased from Sigma-Aldrich and dissolved in the deionized water in concentrations ranging from ppb (ng/mL) to ppm (μg/mL).

B. Sensor Fabrication

Cover glasses with thicknesses of 150 μm were selected as the substrates for fabrication of the arrays of polymer toroid microresonators. Prior to casting a drop of the photoresin solution, a 400 nm layer of the water-matched refractive index adhesive was deposited onto the substrate via spin-coating at 3000 r/min for a duration of 30 s. The substrate was heated at 50°C for 4 h to evaporate the solvent and guarantee a robust contact between the polymer structure and the substrate. The substrate was then cooled down to room temperature and placed into the 2PP setup.

Two-photon polymerization fabrication was performed on the basis of the in-house made setup with a mode locked Ti:Sa laser system (Tsunami, Spectra Physics) with an emission wavelength of 780 nm, a repetition rate of 82 MHz, and a pulse width of 90 fs. The power of the incoming light was controlled by a photodiode and adjusted via a combination of a rotatable $\lambda/2$ retardation plate and a polarizing beamsplitter. The flexibility of the polymerization process in the 3D space is guaranteed by an acousto-optical modulator (AOM) used as a shutter, galvo scanner that allows laser beam redirection in the plane parallel to the substrate, and positioning of the sample in height is enabled by the linear stages. Using an oil-immersed 100× objective with an NA of 1.4, the laser was tightly focused into the photoresin to gain high resolution in the fabrication of the 3D polymer structures. To prevent the mixing of the photosensitive material with the immersion oil, the sample with the photoresin droplet was placed upside-down. The computer-aided design (CAD) model of the microresonator was divided into layers and then the program creates a unique route for the laser beam for each layer.

We optimized the set of illumination parameters to ensure the polymerization of a thousand toroid sensors in a reasonable amount of time. The slicing and hatching distances have been selected as 200 nm and 100 nm, respectively. It was discovered that the speeding up of the laser spot translation up to 100 mm/s for toroid and up to 200 mm/s for the supporting components with a corresponding enhancement of the delivered average laser power till $P_{avr} = 30$ mW does not lead to the formation of structural combs on the cavity rim, which would indicate insufficient voxel overlapping. With this set of parameters, the manufacturing duration for a single microresonator is reduced to less than one minute. A wet chemical treatment was used on the 2PP for 20 min in the 4-methylpentan-2-one developer before the 2PP was submerged for 10 min in 2-propanol to remove the nonpolymerized material. The constructions were finally left in ambient conditions for a number of hours to allow the solvent to dissipate.

C. Measuring Instrument

Sensing with multiple polymer microresonators is based on collimated laser light illumination of the whole area containing cavities. The excitation is via an optical prism, and the radiated light in the far field is detected with a camera (Fig. 1).

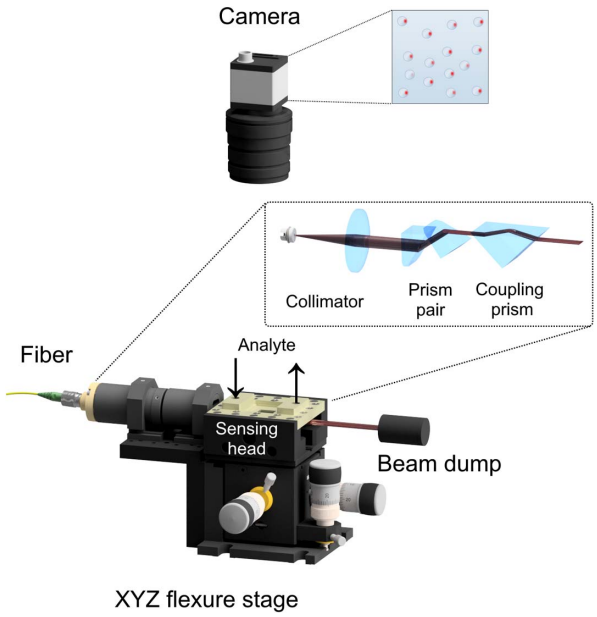

Fig. 1. Main components of the sensing instrument for simultaneous collection of the spectral responses from a multiple polymer microresonator. The excitation laser, wavemeter, and components for the fluid selection and pumping are not depicted.

The sensor excitation part is based on a diode laser (Velocity, New Focus; Newport) that is tunable from 680 to 690 nm with a 200 kHz linewidth. Through the use of suitable single-mode optical fibers (630 HP, Thorlabs) and individual polarization controllers (FPC030, Thorlabs), the laser beam is transmitted to the sensor head in a collimated manner to excite the TE modes. A constant feedback loop to the wavemeter (WS7-30, HighFinesse) with fiber splitters (99%/1%) was introduced to control the laser wavelength. The achromatic optical collimation package (60FC-T-4-M40-24, Schäfter + Kirchhoff) with an output beam diameter of ≈8 mm is used to achieve the illumination of the whole sensing area on the sample at once. An anamorphic prism pair was introduced into the optical path after the collimator to change the incident laser beam profile from circular to elliptical. This compensated the elongation of the collimated beam projection in the propagation direction at the prism excitation surface and ensured a circular shape of the spot on the prism excitation surface. The sensor detection part contained a lens objective and a monochrome high-speed global shutter camera (CB262RG-GP-X8G3, XIMEA). By sweeping the laser wavelength, the spectra are retrieved from the microcavity radiated signal for each resonator in the field of view of the camera where the rise in the radiated intensity corresponds to the resonance conditions.

To stabilize the coupling conditions, an immersion oil was used to obtain the optical contact between the cover glass of the sensor and the optical prism. The sensing head was put together using the prism holder, optical prism, sensor sample, and flow chamber components, and was positioned on a precise three-axis flexure stage. The sensing chamber contains one inlet and one outlet, and forms a single flow channel where all resonators are allocated. The channel shape was numerically optimized in

the COMSOL Multiphysics software to guarantee the uniform delivery of the agent without local fluid turbulence. The chamber was supplemented with the viewing window isolated with the glass plate to control the flow evolution and enable radiated signal collection with the camera. The microfluidic tubing connects the sensing head with the fluid pumping system via the inlet to pump the analyte and with a waste container from the outlet side. The pressure-based controller (LineUp Flow EZ, Fluigent) is used in conjunction with the flow rate sensor (FLOW UNIT, Fluigent) and selection valve (M-SWITCH, Fluigent) to choose liquids from eight separate containers with water at different contamination levels to be pumped through an array of toroids at a regulated speed of 100 μL/min. The ambient temperature variations are measured with the temperature sensor (PT 100) embedded into the sensing head.

3. RESULTS AND DISCUSSION

A. 4D Microresonator Model

The model of the individual microresonator for fabrication with two-photon polymerization is chosen similar to what was reported earlier in Ref. [31]. Its major and minor radii ($R = 21$ μm and $\rho = 1.8$ μm) are numerically optimized to minimize the radiation losses on the microcavity's curvature. With the selected geometry, the radiation limited Q factor approaches the absorption-limited one for the SZ2080 polymer (1.3×10^7) used for manufacturing. To minimize the surface roughness of the microcavity and thus the scattering losses, which predominantly arise due to the cross-linking between the polymer layers, the toroid sensor is supplemented by a flexible support (hinge). It allows fabrication of a toroid sensor using the common layer-wise polymerization strategy and accommodates the demands for different orientations of the microresonator symmetry axis during the polymerization and sensing phases. Further scattering losses are determined by the cross-linking between the polymerization voxels and are minimized by a compromise between the voxel characteristics and focus spot translation speed. An exemplary image of the multiplexed sensor sample with an array of 2PP toroid microcavities that are allocated at the relative offset of 100 μm is represented in Fig. 2.

B. Sensing Performance Optimization

By optimizing the 2PP microresonator geometry and polymerization conditions the intrinsic energy losses have been minimized. The remaining component of the loaded Q factor–the coupling losses–describes the effectiveness of the energy transfer from the external medium to the microcavity. The coupling losses are minimized when the phase-matching conditions and the overlap of the light field between the coupler and the cavity are met. By lining up the coupling frequency with the WGM and the propagation constants in the coupling unit and microcavity, the phase matching is accomplished. For the optical prism coupling scheme, this means equalizing the effective refractive index of the microresonator mode (n_{eff}) with the in-plane prism refractive index (n_c) projection for the excitation beam by $n_{\text{eff}} = n_c \sin\theta$. The modes of the microtoroid have been numerically searched around 680 nm within the prism side incident angles [37°, 45°] in COMSOL Multiphysics

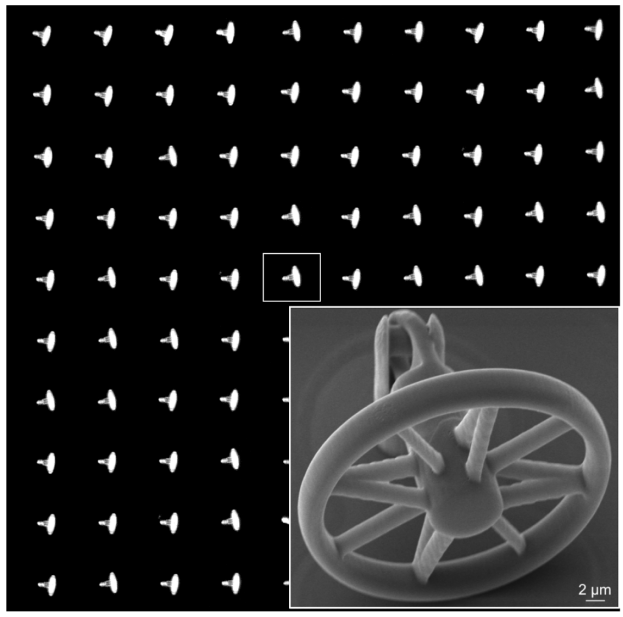

Fig. 2. Overview of the multiplexed sensor with 100 microresonators taken by the measuring system camera. Inset demonstrates an SEM image of the individual microresonator.

[Fig. 3(a)]. The refractive index of the coupling prism N-BK7 is 1.5136 at this wavelength (Schott glass collection database). The incident angle for the upper face of the prism θ is linked to the side incident angle α_{in} for a right-angle prism according to $\theta = \arcsin(\sin\alpha_{\text{in}}/n_c) + 45°$. Results show that the fundamental mode can be excited in the 2PP toroid microcavity with selected geometry: $R = 21$ μm, $\rho = 1.8$ μm, $n_r = 1.502$ (provided by manufacturer) at $\alpha_{\text{in}} = 45°$. By decreasing the angle, the efficient excitation of the higher-order modes is expected, where Q_{rad} for higher order modes drops from $\sim 10^7$ ($\alpha_{\text{in}} = 45°$) down to $\sim 10^5$ ($\alpha_{\text{in}} = 37°$). The sensitivity to changes of the bulk refractive index in arbitrary units (RIU) varies insignificantly, where for the fundamental TE mode it does not exceed 20 nm/RIU. Combination of the illumination

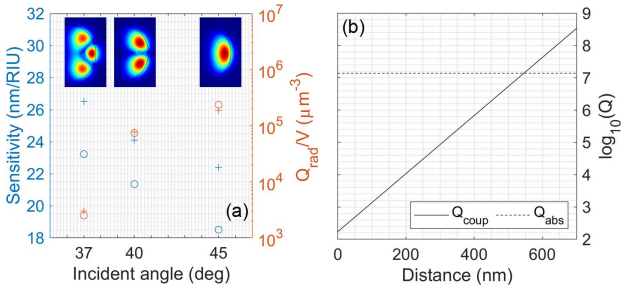

Fig. 3. Numerical results of the optimization of the coupling-limited Q factor for the right-angle prism coupling scheme. (a) Impact of the incident angle α_{in} on the sensitivity and Q_{rad}/V ratio for the modes (circle, TE; cross, TM polarization) of different orders excited in the microcavity around 680 nm. Insets demonstrate distribution of the EM field for TE modes phase matched at $\alpha_{\text{in}} = 37°$, 40°, and 45°. (b) Variations of the coupling-limited Q factor (Q_{coup}, solid line) and absorption-limited Q factor (Q_{abs}, dashed line) for different gaps between the coupling unit and microresonator.

angle of 45° with the right-angle prism simplifies the overall geometry of the illumination optical path and enables exceptional mechanical robustness.

An overlap between the evanescent fields can be adjusted by changing the distance between the coupler (prism) and the microresonator. The variations of the coupling-limited Q factor have been numerically studied according to the equation for the optical prism coupling scheme derived in Ref. [37]. The results represented in Fig. 3(b) show that without a gap between the coupling prism and microresonator, the maximum possible loaded Q-factor does not exceed 10^3. With a gap increasing the losses drop so that at 200 nm distance the loaded Q factor may exceed 10^4, and at 400 nm it reaches $\sim 10^6$. The coupling limited Q factor approaches the fundamental limit for absorption at a distance of more than 550 nm.

For the chosen sensor configuration, the gap can be ensured by the adhesive layer with the same refractive index as the intended external environment (water). However, the deposition of such a layer is possible only before the polymerization; therefore, it would impact the photopolymerization process during the microcavities fabrication. The variations of the polymerization voxel caused by a thin distancing layer has been numerically studied using the model that describes the variations of the polymerization voxel dimensions when the 2PP illumination path lies through multiple layers with different optical properties [38].

A multilayer structure consisting of $m + 1 = 4$ layers, immersion oil (0), glass substrate (1), water-matched polymer layer (2), and photoresin (3), is simulated. The pulsed laser settings are: wavelength $\lambda = 780$ nm, pulse duration $\tau = 90$ fs, repetition frequency $f_{rep} = 82$ MHz, average power $P_{avr} = 30$ mW, laser spot translation speed equals 100 mm/s, and polarization is linear, aligned along the X axis. The 100× magnification objective lens has been selected with NA = 1.4, $f = 200$ μm. The refractive index of the material for the distancing layer is set to $n_2 = 1.328 - 6.2 \times 10^{-7} i$ (MyPolymer MY-133MC) and refractive index for other materials are $n_0 = 1.518$, $n_1 = 1.5168$, and $n_3 = 1.502$. Thickness of the glass substrate is $t_1 = 150$ μm which is supposed to have a perfect plain surface ($\sigma_1 = 0$). The thickness of the distancing film has been varied within the value of the wavelength (from 0 to 700 nm). The calculation region has been limited by 0.8 μm for X and Y, and by 3 μm for Z coordinate with the grid size of $\lambda/100$.

It has been calculated that the light transmission level remains at ≈90% with reflection of up to 10% (absorption can be neglected) for the thickness of the water-matched layer within one wavelength. The essential portion of the energy that is reflected back enables enhancement in accuracy of the substrate/photoresin plane localization that is one of the most critical aspects limiting the 2PP manufacturing repeatability [39]. In turn, this prevents missing microresonators in the array due to the lack of contact with the substrate (washed out during the development) or damage to the underside (submerged into the substrate). The variations of the characteristic length of the polymerization voxel (volume cube root) along the whole polymerization depth valid for the chosen microresonator geometry (0–43 μm) are represented in Fig. 4.

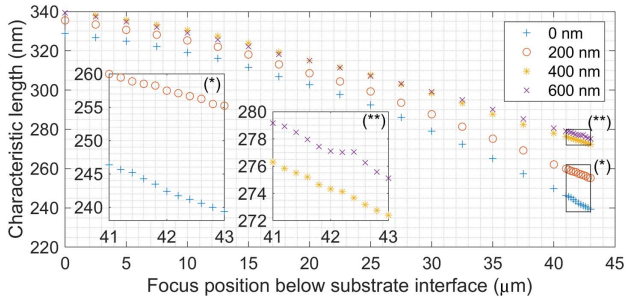

Fig. 4. Results of the numerical estimations of the deviations of the polymerization voxel characteristic length for different thicknesses of the water-matched adhesive film (0, 200, 400, 600 nm) between the substrate and photosensitive material in the 2PP process.

The mean power of the laser is tuned for different thicknesses of the distancing layer to compensate the reflected energy and equalize the energy delivered to the photosensitive material. Particularly, this means an increase in the laser mean power (relative to the case without distancing layer) by 12.5%, 10%, and 4.5% for 600, 400, and 200 nm thick film, correspondingly. The results show that the voxel length continuously declines with the distance to the substrate and the character of variations for the illumination configuration with water-matched layer is in accordance with the one without the additional distancing layer. An impact of the thin adhesive film is determined to be insignificant, where the major voxel length deviations are linked to the refractive index mismatch between the glass substrate, immersion oil, and photoresin material. At the same time, the variations of the characteristic voxel size remains limited by 5 nm around the region of [41,43] μm, where the material is illuminated to form a microresonator for illumination configuration with the adhesive film. According to the model that estimates the scattering losses limited Q factor (Q_{scat}) as a function of the varying relative permittivity proposed in Ref. [40], the determined level of variations of the voxel characteristics ensures $Q_{scat} \sim 10^6$. This ensures the ability to produce the high-quality polymer surfaces with optical quality even in the presence of a subwavelength distancing layer.

To form a homogeneous distancing layer with a thickness of several hundred nanometers, the viscosity of the original water-matched polymer (MyPolymer MY-133MC) has been reduced by mixing with a solvent. Adhesive solutions at different proportions with the solvent starting from 1:15 up to 1:80 were deposited onto the substrate and spin-coated at 3000 r/min over 30 s. Then, the thicknesses of the layers were analyzed with the white light interferometer, where the layer was locally removed for several samples from the batch and additionally sputtered to enhance the contrast. It has been determined that the 1:15 and 1:16 solutions lead to formation of the distancing layer with thickness above the laser wavelength, whereas for the 1:80 solution no layer was created. For the 1:18 solution, the mean thickness of the distancing layer is measured at ≈550 nm, the 400 nm layer distancing layer is measured for a 1:22 solution, the 300 nm layer for a 1:26 solution, and the 200 nm layer is measured for a 1:30 solution. It has been

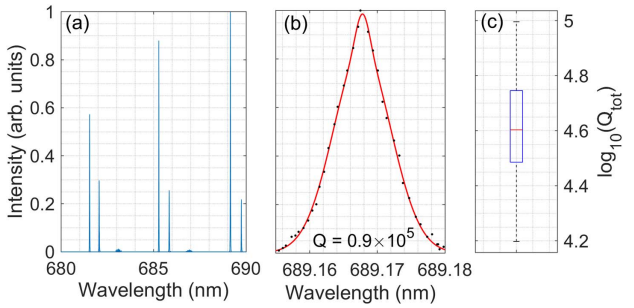

Fig. 5. Spectral resonance properties of the 2PP toroid microresonator fabricated on a sample with a 400 nm gap to the substrate. (a) Overview of the resonance lines for the exemplary microresonator within the 10 nm spectral range measured in water. (b) Zoom into the resonance line with a sharp peak. (c) Statistics on the measured loaded quality factor in a water environment for 100 microresonators on a single sample.

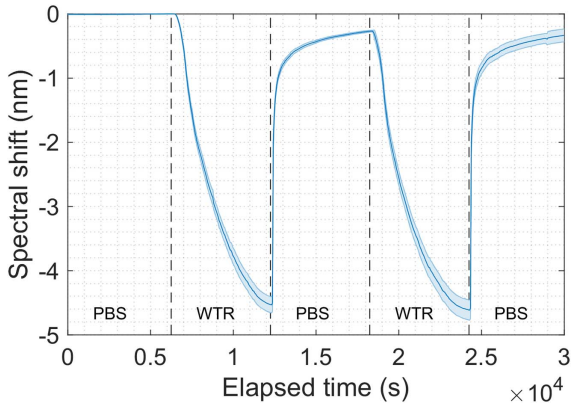

Fig. 6. Evidence of the 4D sensing enabled by exemplary sample of the multiplexed sensor with 529 units of 2PP microresonators in the form of the long-term dynamics of the spectral shift for the periodically varied environment between water (WTR) and phosphate buffered saline (PBS). The solid line shows the spectral shift mean value; shaded area is the 95% confidence interval.

determined that by increasing the gap, the observed loaded Q factor in the water can be increased by two orders of magnitude. For a distance of 400 nm, where the theoretical limits for scattering and coupling losses match ($Q = 10^6$), the upper limit for the loaded Q factor of 2PP resonators has been measured at the level of 10^5 (Fig. 5). Despite the accuracy on the order of tens of nanometers for positioning and structuring during 2PP fabrication, the toroid resonators still exhibit spectral deviations with a median value of 4×10^4, where it drops down to 2×10^4 for particular resonances. Further distancing of the toroids from the substrate does not enhance the loaded Q factors, but results in more microcavities without detectable resonance behavior with less than 5% of the toroids showing a signal for a 550 nm gap. The impossibility to reach the theoretical limit is expected to be caused by further scattering losses on the imperfections of the toroidal rim and polymer inhomogeneities.

C. 4D Sensing with 2PP Resonators

The use of the 2PP microresonators fabricated out of the SZ2080 material is particularly attractive due to the self-sensing effect of the microresonator structure that enables realization of the 4D printed sensor system. The mechanism of self-sensing arises from swelling and shrinking forces that act on resonator geometry when immersed in different liquids. Particularly, when being immersed in the wetting solvents, the molecules of the latter start to penetrate into the polymer structure, which leads to resonator expansion. When changing the environment to the non-wetting solvent (e.g., water), the penetrated molecules can be extracted and material shrinks. Here, the overall gain for sensitivity relative to the numerical estimations for the pure evanescent field interaction (≈20 nm/RIU, see Fig. 3) can rise by orders of magnitude. Moreover, the efficiency of the self-sensing phenomenon tends to grow when repeatedly inducing the sequential swelling and shrinking of microresonators, but after several repetitions of swelling/shrinking actions the behavior stabilizes. The spectral response of the multiplexed 4D sensor (averaged over 23×23 multiplexed sensor units) for three repetitions in a row on the measurement of the phosphate buffered saline (PBS) solutions and water is represented in Fig. 6.

The results show a clear distinction of the represented spectral shift variations against the expected step-like changes with short-term (~300 s) dynamics for mixing the liquids in the sensing chamber in the case of pure bulk refractive index sensing. Except for the first phase of PBS pumping with constant spectral response (sensors kept in PBS overnight before start of the measurement), the detected spectral shift variations show clear long-term dynamics for all phases, where the saturation is not reached within a phase. At the same time, the stability of the initial PBS state serves as a saturation level indicator for PBS measurement phases. The magnitude of the averaged spectral shift exceeds 4 nm over 6000 s of solution pumping that compared to ≈40 pm of spectral shift for the bulk refractive index difference between PBS and water stands for swelling of the microresonators in PBS and their shrinkage in water. We have also observed the acceptable reproducibility of the mean spectral shift dynamics for water and PBS among repetitions, whereas the difference in sensing performance between microresonators leads to an increase in the confidence interval with time after the beginning of the experiment. This is linked to the varying spectral properties of the individual 2PP microresonators.

D. Perfluoroalkyl Substances Detection

At first, the microresonator response to PFAS chemicals is tested within the experiments where the environment in the sensing cell is sequentially changed from the clean deionized to PFOA contaminated water. Within these trials the relatively high levels of contaminations (0.1–10 ppm) have been used. Unlike the averaged spectral shift, the spectral response (generalized) is retrieved hereinafter as the first principle component (PC1), which is a linear combination of the spectral shift dynamics among all resonators and follows the most prominent variance in the dataset. Such a representation of the spectral variations is advantageous to account for the different sensitivities of the microresonators and to reduce the impact of local variations/noises that is classified via the principle component

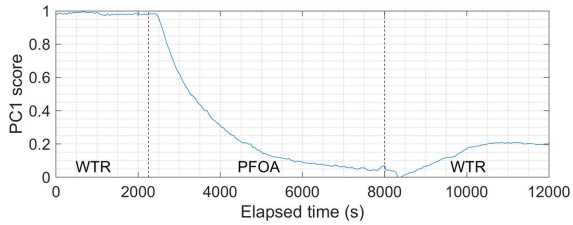

Fig. 7. Spectral response of the multiplexed 4D microresonator sensor in the form of the scaled PC1 value (PC1 score) for a 10 ppm PFOA solution followed by the pure water (WTR) flushing.

analysis (PCA) as an insignificant component. It has been determined that the generalized spectral shift of the microresonators remains implicit with respect to the pure water for concentration up to 10 ppm. When changing water to 10 ppm PFOA, the generalized response shows a clear negative trend that indicates microresonator shrinkage induced by PFOA molecules (Fig. 7).

The measured spectral shift negative dynamics tends to reach a constant level at ≈6000 s after starting the pumping of the PFOA contaminated water. When the sensing chamber is refilled with clean water next to the PFOA, the level of the generalized spectral response rises, but it does not recover to the initial water level. This is assumed to be related to the compression limit for the microresonator and the common character of the material response for pure water and PFOA (it tends to shrink). Therefore, the microcavity pre-swelling is expected to improve the PFAS sensitivity and this can be done via pumping the PBS solutions (see Fig. 6). For this reason, the experiment has been designed so that the PBS is pumped for 6000 s before the PFAS sensing and prior to the first phase of PFAS sensing, the pure water was pumped for the same duration to get the identical state of the 4D microresonator.

The results of the spectral variations when incubating a multiplexed 4D sensor in increasing concentrations of PFOA and PFBS solutions in the range from 1 ppb to 20 ppm are represented in Fig. 8. Since both pure and contaminated water will initiate cavity shrinkage, the characteristic dynamical changes measured for a PFAS-containing solution have been compared to the one for pure water. To ensure that the sensing response of the microresonator does not alter with multiple runs of PFAS solution pumping, the water response has been measured before (WTR1) and after multiple interactions with contaminated water (WTR2). To enable the comparison of PFAS-initiated dynamics that have been measured in the different experimental runs, the generalized spectral shift has been scaled.

We determined that the presence of a small amount of PFOA or PFBS in water at the level of 10 ppb and 1 ppb correspondingly leads to changes in the dynamics of the spectral variations relative to the uncontaminated water. The more PFAS components are added to the water, the higher the negative slope in dynamics is, which indicates an acceleration of the shrinkage process in the presence of PFAS chemicals. Unlike PFBS, the difference between the pure water and PFOA-containing water is clearly seen already at the first stages of the shrinkage process, but the difference in dynamics for various levels of PFBS contamination shows up only after hundreds of seconds of pumping the solutions through the sensor. In addition to the rise of the negative slope, the shape of the trend changes with the PFAS concentration. For large concentrations (at the level of ppm), we have observed the appearance of a two-phase trend with acceleration in dynamics of the sensor response in the first phase and deceleration in the second phase compared to the one for water. Here, for the first phase, the difference between concentrations is more expressed than for the second phase and the transition point between the phases occurs earlier when increasing the concentration. For PFBS, the transition point for 0.5 ppm appears at ≈2600 s, whereas for 1 ppm it is already at ≈2100 s. In general, the sensor is more sensitive to PFBS than to PFOA contaminations, where the sensor responses are comparable between 10 ppm PFOA and 0.5 ppm PFBS as well as between 20 ppm PFOA and 1 ppm PFBS, respectively.

The measured spectral response of 4D microresonators to the presence of PFAS molecules can primarily be attributed to the synergistic effect, which occurs when several factors for the interaction of PFAS with polymer material act together. Due to the presence of the radical quencher (DMAEMA) in the two-photon polymerization process, which becomes a part of the polymer chain, the resulting microresonators contain amine functional groups. Materials with amine functional groups exhibit the potential to couple with the anionic PFAS, which

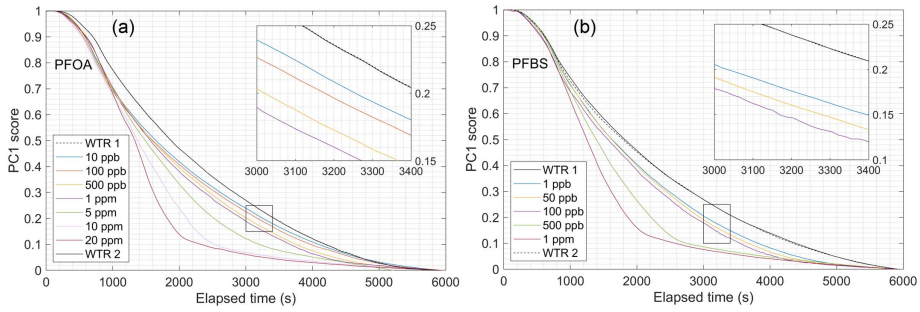

Fig. 8. Dynamical variations of the generalized sensor response in the form of the scaled PC1 for different concentrations of continuously pumped water-based solutions containing different PFAS at varied concentrations. Each variation is measured after the PBS pumping phase for 6000 s. The spectral shift dynamics in pure water before (WTR1) and after (WTR2) the measurements of PFAS are added to each curve. (a) Reaction of the PFOA solutions with concentrations from 10 ppb to 20 ppm. (b) Reaction of the PFBS solutions with concentrations from 1 ppb to 1 ppm.

include the chemicals being tested [41]. First of all, the interaction of the amine-containing material and PFAS molecules is electrostatic and hydrophobic in nature, but microresonator morphology and porosity also impact the sensor response. The amines of the polymer and the carboxylate or sulfonate headgroup of the anionic PFAS are expected to interact electrostatically, where the pH value of the solution strongly impacts the process: the lower the pH, the stronger the interaction. The hydrophobic interactions are determined by the type of the head functional group, PFAS chain length, and hydrophobicity of the microresonator material. It has been reported that PFAS chemicals with sulfonic headgroups (PFBS) have a better adsorption capability than the ones with carboxylic headgroups (PFOA) of the same carbon number [42]. In another work [43], where PFAS chemicals of different chain lengths were compared, it was revealed that the adsorption of the longer-chain compounds is always higher than their shorter-chain counterparts. There are two explanations: the first points to the fact that the long-chain PFAS interact both electrostatically and hydrophobically, while short-chain ones primarily interact electrostatically; the second one addresses the increased potential of the multilayer formation for long-chain PFAS. Morphology and porosity of the material are crucial for PFAS diffusion dynamics and accessibility of the adsorption sites, where a lower material surface area and/or long-chain chemicals result in slower kinetics [44]. Particularly, the increased efficiency in the sensing of the PFBS components compared to PFOA is expected to be linked to the length of the chain. Being a longer-chain compound, PFOA is expected to be less able to penetrate into the nanopores of the microresonator and thus the speed of the material shrinkage is less than for PFBS. For high PFAS concentrations, the role of the small variance in the bulk refractive index of solutions, which is related to the chemical composition of the perfluorinated compounds, rises [6]. This is expressed by the appearance of the two-phase dynamics for higher concentrations of the PFAS components, which is expected to be related to a slight decrease in the bulk refractive index of the solutions. This governs the difference in dynamics between the same concentrations of PFOA and PFBS (in the range of ppm), where the latter shows faster resonator shrinkage.

4. CONCLUSION

In this paper, we demonstrated for what we believe, to the best of our knowledge, was the first time that an optical microresonator sensor was used to detect per- and polyflouroalkyl water contaminants. The sensor was constructed in a multiplexed imaging configuration with multiple hundreds of 4D microcavities fabricated with two-photon polymerization that enable enhanced sensitivity thanks to the material reaction on the external medium (self-sensing). The paper presents a list of numerical and experimental improvements implemented in the fabrication of an array of 2PP microresonators that improve the spectral response by up to two orders of magnitude for a 4D sensor compared to its 3D counterpart and demonstrate a loaded quality factor in water of $\sim 10^5$. The performance in the detection of PFAS contaminations in water has been tested using the example of two representatives of the class of anionic substances with different functional groups and chain lengths (PFOA and PFBS). We demonstrated that concentrations of 1 ppb for PFBS and 10 ppb for PFOA are detectable without applying selective layers onto microresonators. Given the key advantages of the microresonator-based optical sensors, the applicability of this approach is expected to boost the registration of the persistent water contaminants. With further studies on the host material for the 4D microresonator unit, it is expected to be potentially feasible to implement an integrated approach to solve the problem of aqueous environment contamination by PFAS with simultaneous detection of the initial contamination and efficient removal of small PFAS concentrations.

Funding. Bundesministerium für Bildung und Forschung (03VP08220).

Acknowledgment. We would like to acknowledge the group of Dr. Maria Farsari (IESL-FORTH), and particularly Dr. Gordon Zyla, for providing the photoresin. Authors Andreas Ostendorf and Anton Saetchnikov are grateful to the BMBF for partly funding this work under the VIP +-Programme in the project IntellOSS. We acknowledge support by the Open Access Publication Funds of the Ruhr-Universität Bochum.

Disclosures. The authors declare no conflicts of interest.

Data Availability. Data underlying the results presented in this paper are not publicly available at this time but may be obtained from the authors upon reasonable request.

REFERENCES

1. S. F. Nakayama, M. Yoshikane, Y. Onoda, Y. Nishihama, M. Iwai-Shimada, M. Takagi, Y. Kobayashi, and T. Isobe, "Worldwide trends in tracing poly- and perfluoroalkyl substances (PFAS) in the environment," TRAC Trends Anal. Chem. **121**, 115410 (2019).
2. H. Fiedler, T. Kennedy, and B. J. Henry, "A critical review of a recommended analytical and classification approach for organic fluorinated compounds with an emphasis on per- and polyfluoroalkyl substances," Integr. Environ. Assess. Manage. **17**, 331–351 (2021).
3. M. Ateia, A. Maroli, N. Tharayil, and T. Karanfil, "The overlooked short- and ultrashort-chain poly- and perfluorinated substances: a review," Chemosphere **220**, 866–882 (2019).
4. B. F. Scott, C. A. Moody, C. Spencer, J. M. Small, D. C. G. Muir, and S. A. Mabury, "Analysis for perfluorocarboxylic acids/anions in surface waters and precipitation using GC–MS and analysis of PFOA from large-volume samples," Environ. Sci. Technol. **40**, 6405–6410 (2006).
5. H. Ryu, B. Li, S. de Guise, J. McCutcheon, and Y. Lei, "Recent progress in the detection of emerging contaminants PFASs," J. Hazard. Mater. **408**, 124437 (2021).
6. N. Cennamo, G. D'Agostino, G. Porto, A. Biasiolo, C. Perri, F. Arcadio, and L. Zeni, "A molecularly imprinted polymer on a plasmonic plastic optical fiber to detect perfluorinated compounds in water," Sensors **18**, 1836 (2018).
7. N. Cennamo, L. Zeni, P. Tortora, M. E. Regonesi, A. Giusti, M. Staiano, S. D'Auria, and A. Varriale, "A high sensitivity biosensor to detect the presence of perfluorinated compounds in environment," Talanta **178**, 955–961 (2018).
8. R. Pitruzzella, F. Arcadio, C. Perri, D. Del Prete, G. Porto, L. Zeni, and N. Cennamo, "Ultra-low detection of perfluorooctanoic acid using a novel plasmonic sensing approach combined with molecularly imprinted polymers," Chemosensors **11**, 211 (2023).

9. G. Moro, F. Chiavaioli, S. Liberi, P. Zubiate, I. Del Villar, A. Angelini, K. de Wael, F. Baldini, L. M. Moretto, and A. Giannetti, "Nanocoated fiber label-free biosensing for perfluorooctanoic acid detection by lossy mode resonance," Results Opt. **5**, 100123 (2021).
10. F. Faiz, G. Baxter, S. Collins, F. Sidiroglou, and M. Cran, "Polyvinylidene fluoride coated optical fibre for detecting perfluorinated chemicals," Sens. Actuators B Chem. **312**, 128006 (2020).
11. V. B. Braginsky, M. L. Gorodetsky, and V. S. Ilchenko, "Quality-factor and nonlinear properties of optical whispering-gallery modes," Phys. Lett. A **137**, 393–397 (1989).
12. K. J. Vahala, "Optical microcavities," Nature **424**, 839–846 (2003).
13. X. Jiang, A. J. Qavi, S. H. Huang, and L. Yang, "Whispering-gallery sensors," Matter **3**, 371–392 (2020).
14. M. R. Foreman, J. D. Swaim, and F. Vollmer, "Whispering gallery mode sensors," Adv. Opt. Photonics **7**, 168–240 (2015).
15. L. Cai, J. Pan, Y. Zhao, J. Wang, and S. Xiao, "Whispering gallery mode optical microresonators: structures and sensing applications," Phys. Status Solidi A **217**, 1900825 (2020).
16. D. Yu, M. Humar, K. Meserve, R. C. Bailey, S. N. Chormaic, and F. Vollmer, "Whispering-gallery-mode sensors for biological and physical sensing," Nat. Rev. Methods Primers **1**, 83 (2021).
17. B. Özel, R. Nett, T. Weigel, G. Schweiger, and A. Ostendorf, "Temperature sensing by using whispering gallery modes with hollow core fibers," Meas. Sci. Technol. **21**, 094015 (2010).
18. J. Su, A. F. Goldberg, and B. M. Stoltz, "Label-free detection of single nanoparticles and biological molecules using microtoroid optical resonators," Light Sci. Appl. **5**, e16001 (2016).
19. M. Eryürek, Z. Tasdemir, Y. Karadag, S. Anand, N. Kilinc, B. E. Alaca, and A. Kiraz, "Integrated humidity sensor based on SU-8 polymer microdisk microresonator," Sens. Actuators B Chem. **242**, 1115–1120 (2017).
20. A. V. Saetchnikov, E. A. Tcherniavskaia, V. V. Skakun, V. A. Saetchnikov, and A. Ostendorf, "Reusable dispersed resonators-based biochemical sensor for parallel probing," IEEE Sens. J. **19**, 7644–7651 (2019).
21. C. Lemieux-Leduc, R. Guertin, M.-A. Bianki, and Y.-A. Peter, "All-polymer whispering gallery mode resonators for gas sensing," Opt. Express **29**, 8685–8697 (2021).
22. J. Liao and L. Yang, "Optical whispering-gallery mode barcodes for high-precision and wide-range temperature measurements," Light Sci. Appl. **10**, 32 (2021).
23. A. V. Saetchnikov, E. A. Tcherniavskaia, V. A. Saetchnikov, and A. Ostendorf, "Deep-learning powered whispering gallery mode sensor based on multiplexed imaging at fixed frequency," Opto-Electron. Adv. **3**, 200048 (2020).
24. A. V. Saetchnikov, E. A. Tcherniavskaia, V. A. Saetchnikov, and A. Ostendorf, "Intelligent optical microresonator imaging sensor for early stage classification of dynamical variations," Adv. Photonics Res. **2**, 2100242 (2021).
25. F. Vollmer, D. Braun, A. Libchaber, M. Khoshsima, I. Teraoka, and S. Arnold, "Protein detection by optical shift of a resonant microcavity," Appl. Phys. Lett. **80**, 4057–4059 (2002).
26. Y. Chen, Y. Yin, L. Ma, and O. G. Schmidt, "Recent progress on optoplasmonic whispering-gallery-mode microcavities," Adv. Opt. Mater. **9**, 2100143 (2021).
27. M. P. Serrano, S. Subramanian, C. von Bilderling, M. Rafti, and F. Vollmer, "'Grafting-to' covalent binding of plasmonic nanoparticles onto silica WGM microresonators: mechanically robust single-molecule sensors and determination of activation energies from single-particle events," Sensors **23**, 3455 (2023).
28. T. Reynolds, N. Riesen, A. Meldrum, X. Fan, J. M. M. Hall, T. M. Monro, and A. François, "Fluorescent and lasing whispering gallery mode microresonators for sensing applications," Laser Photonics Rev. **11**, 1600265 (2017).
29. N. Toropov, G. Cabello, M. P. Serrano, R. R. Gutha, M. Rafti, and F. Vollmer, "Review of biosensing with whispering-gallery mode lasers," Light Sci. Appl. **10**, 42 (2021).
30. W. Chen, Ş. Kaya Özdemir, G. Zhao, J. Wiersig, and L. Yang, "Exceptional points enhance sensing in an optical microcavity," Nature **548**, 192–196 (2017).
31. A. V. Saetchnikov, E. A. Tcherniavskaia, V. A. Saetchnikov, and A. Ostendorf, "A laser written 4D optical microcavity for advanced biochemical sensing in aqueous environment," J. Lightwave Technol. **38**, 2530–2538 (2020).
32. Y. S. Lui, W. T. Sow, L. P. Tan, Y. Wu, Y. Lai, and H. Li, "4D printing and stimuli-responsive materials in biomedical aspects," Acta Biomater. **92**, 19–36 (2019).
33. A. Mitchell, U. Lafont, M. Hołyńska, and C. Semprimoschnig, "Additive manufacturing — a review of 4D printing and future applications," Addit. Manuf. **24**, 606–626 (2018).
34. A. Ovsianikov, A. Ostendorf, and B. N. Chichkov, "Three-dimensional photofabrication with femtosecond lasers for applications in photonics and biomedicine," Appl. Surf. Sci. **253**, 6599–6602 (2007).
35. Y. Xu, P. Bai, X. Zhou, Y. Akimov, C. E. Png, L.-K. Ang, W. Knoll, and L. Wu, "Optical refractive index sensors with plasmonic and photonic structures: promising and inconvenient truth," Adv. Opt. Mater. **7**, 1801433 (2019).
36. I. Sakellari, E. Kabouraki, D. Gray, V. Purlys, C. Fotakis, A. Pikulin, N. Bityurin, M. Vamvakaki, and M. Farsari, "Diffusion-assisted high-resolution direct femtosecond laser writing," ACS Nano **6**, 2302–2311 (2012).
37. M. L. Gorodetsky and V. S. Ilchenko, "Optical microsphere resonators: optimal coupling to high-*Q* whispering-gallery modes," J. Opt. Soc. Am. B **16**, 147–154 (1999).
38. A. Saetchnikov, V. Saetchnikov, E. Tcherniavskaia, and A. Ostendorf, "Effect of a thin reflective film between substrate and photoresin on two-photon polymerization," Addit. Manuf. **24**, 658–666 (2018).
39. M. Malinauskas, M. Farsari, A. Piskarskas, and S. Juodkazis, "Ultrafast laser nanostructuring of photopolymers: a decade of advances," Phys. Rep. **533**, 1–31 (2013).
40. M. L. Gorodetsky, A. D. Pryamikov, and V. S. Ilchenko, "Rayleigh scattering in high-*Q* microspheres," J. Opt. Soc. Am. B **17**, 1051–1057 (2000).
41. M. Ateia, A. Alsbaiee, T. Karanfil, and W. Dichtel, "Efficient PFAS removal by amine-functionalized sorbents: critical review of the current literature," Environ. Sci. Technol. Lett. **6**, 688–695 (2019).
42. Z. Du, S. Deng, Y. Bei, Q. Huang, B. Wang, J. Huang, and G. Yu, "Adsorption behavior and mechanism of perfluorinated compounds on various adsorbents–a review," J. Hazard. Mater. **274**, 443–454 (2014).
43. E. Gagliano, M. Sgroi, P. P. Falciglia, F. G. A. Vagliasindi, and P. Roccaro, "Removal of poly- and perfluoroalkyl substances (PFAS) from water by adsorption: role of PFAS chain length, effect of organic matter and challenges in adsorbent regeneration," Water Res. **171**, 115381 (2020).
44. Q. Yu, R. Zhang, S. Deng, J. Huang, and G. Yu, "Sorption of perfluorooctane sulfonate and perfluorooctanoate on activated carbons and resin: kinetic and isotherm study," Water Res. **43**, 1150–1158 (2009).